

A novel blind deconvolution de-noising scheme in failure prognosis

Bin Zhang¹, Taimoor Khawaja², Romano Patrick¹,
George Vachtsevanos^{1,2}, Marcos Orchard³ and
Abhinav Saxena²

¹Impact Technologies, LLC, Rochester, NY 14623, USA

²School of Electrical and Computer Engineering, Georgia Institute of Technology, Atlanta, GA 30332, USA

³Electrical Engineering Department, University of Chile, Av. Tupper 2007, Santiago, Chile

With increased system complexity, condition-based maintenance (CBM) becomes a promising solution for system safety by detecting faults and scheduling maintenance procedures before faults become severe failures resulting in catastrophic events. For CBM of many mechanical systems, fault diagnosis and failure prognosis based on vibration signal analysis are essential techniques. Noise originating from various sources, however, often corrupts vibration signals and degrades the performance of diagnostic and prognostic routines, and consequently, the performance of CBM. In this paper, a new de-noising structure is proposed and applied to vibration signals collected from a testbed of the main gearbox of a helicopter subjected to a seeded fault. The proposed structure integrates a blind deconvolution algorithm, feature extraction, failure prognosis and vibration modelling into a synergistic system, in which the blind deconvolution algorithm attempts to arrive at the true vibration signal through an iterative optimization process. Performance indexes associated with quality of the extracted features and failure prognosis are addressed, before and after de-noising, for validation purposes.

Key words: blind deconvolution; condition-based maintenance; de-noise; failure prognosis; planetary gear carrier; vibration.

Address for correspondence: Bin Zhang, Impact Technologies, LLC, Rochester, NY 14623, USA.
E-mail: bin.zhang@impact-tek.com
Figures 2, 3 and 9–23 appear in colour online: <http://tim.sagepub.com>

Nomenclature

f^s	Planetary carrier rotation frequency
N_t	Number of teeth in the annular gear
p	Index of gear in consideration
N_p	Number of gears
m	Index of harmonics of tooth meshing frequency
M	Total number of tooth meshing harmonics in consideration
N	Index of harmonics of carrier rotation frequency
N	Total number of carrier rotation harmonics in consideration
Δ	Angular phase shift caused by a crack on the plate
α_n	Magnitude of modulating signal at its harmonic nf^s
β_m	Magnitude of vibration signal from a single gear at its harmonic $mN_t f_s$
$\varphi_{p,m,n}$	Magnitude of frequency components from gear p at sideband $mN_t + n$
H	Remainder of $(mN_t + n)/N_p$
$\lambda_{m,n}$	Magnitude of combined vibration signal (superposition of vibration signals from different gears) at sideband $mN_t + n$
$\bar{\theta}$	Angular phase evenly separated by N_p gears
$W_{m,n}$	Weighting factor of non-linear projection at sideband $mN_t + n$
θ_p	Angular position of gear p

1. Introduction

The increasing demand for system safety and reliability requires that faults in complex dynamic systems be detected and isolated as early as possible so that maintenance practices can be scheduled before faults become severe. Traditional breakdown and scheduled maintenance practices are, therefore, replaced by condition-based maintenance (CBM) to meet this need (Vachtsevanos *et al.*, 2006). CBM is an integration of signal processing, feature extraction, fault detection and isolation, failure prognosis, and decision-making. In order to implement CBM, the health of critical components and subsystems must be monitored and reliable diagnostic/prognostic strategies developed (Vachtsevanos *et al.*, 2006). Then, the system health can be assessed and maintenance practices can be scheduled based on the remaining useful life of components/systems to avoid catastrophic events.

Performance of failure prognostic routines, however, is closely related to the features (also known as condition indicators) derived from sensor data, which reveal the evolution and propagation of a failure in the system (Lebold *et al.*, 2000; Saxena *et al.*, 2005; Wu *et al.*, 2004, 2005). For many mechanical systems, features are typically extracted from vibration data (Keller and Grabill, 2003). During the operation of such a system, if a fault occurs, it is expected that the vibration signals will exhibit a characteristic signature, which reveals the severity and location of the fault. Noise in the system, however, often corrupts the vibration signals and masks the indication of faults, especially in their early stages, thus curtailing the ability to diagnose and predict failures accurately. Therefore, it is important to develop a good and reliable

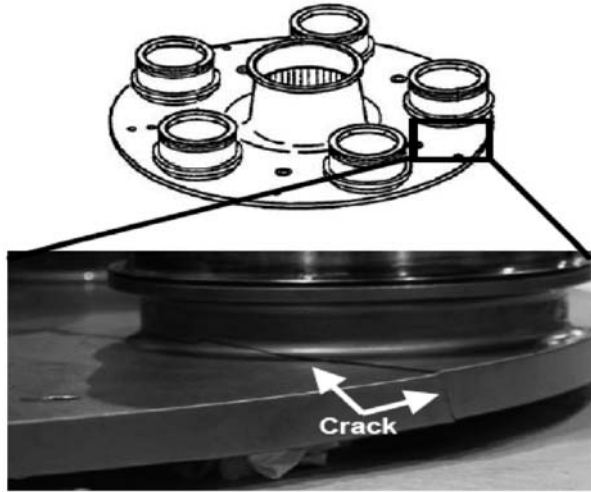


Figure 1 The crack of planetary gear carrier plate of the UH-60A helicopter

de-noising scheme to improve the signal-to-noise ratio and make the characteristics of the fault perceptible in the vibration data. This process will improve the quality of the obtained features, potentially lower the fault detection threshold while increasing the accuracy of the diagnostic and prognostic algorithms.

The main transmission of Blackhawk and Seahawk helicopters employs a five-planet epicyclic gear system, which is a critical component directly related to the availability and safety of the vehicle (Keller and Grabill, 2003; McFadden and Smith, 1985). Recently, a crack in the planetary carrier plate was discovered during regular maintenance, as shown in Figure 1. This resulted in major overhaul, re-design and replacement of gear plates with a high cost associated with these activities. Manual inspection of all transmissions is not only costly, but also time prohibitive (Saxena *et al.*, 2005). CBM could provide a cost-effective solution for reducing the work burden and enhancing vehicle safety (Saxena *et al.*, 2005). Many research efforts towards designing and implementing CBM on helicopters, such as vibration signal preprocessing (Szczepanik, 1989; Wu *et al.*, 2004), vibration signal modelling (Patrick, 2006), features extraction (Wu *et al.*, 2004, 2005), detection of cracks, and prediction of crack length (Orchard, 2006), have been carried out. The objective of this paper is to propose a new vibration pre-processing structure, which synergizes vibration de-noising, vibration modelling, feature extraction and failure prognosis, to enhance the performance of CBM. The planetary gear system with a seeded crack on the gear carrier plate will be used to verify the proposed method.

For an epicyclic gear system, the widely used de-noising technique is time synchronous averaging (TSA), which can be implemented in the time or frequency

domain (Keller and Grabill, 2003; Lebold *et al.*, 2000; Szczepanik, 1989; Wu *et al.*, 2004, 2005). This operation enhances the components at the frequencies that are multiples of the shaft frequency, which are often related to the meshing of gear teeth (Wu *et al.*, 2004, 2005). At the same time, it tends to average out external random disturbances and noise that are asynchronous with the rotation of the gear.

Other de-noising algorithms include blind source separation (BSS; Antoni, 2005; Ayers and Dainty, 1988; Gelle *et al.*, 2000), stochastic resonance (Klamecki, 2005), and adaptive schemes (Antoni and Randall, 2004; Hillerstrom, 1996). BSS aims to extract individual, but physically different, excitation sources from the combined output measurement (Antoni, 2005). Because of the complex environment and the large number of noise sources in mechanical systems, the application of BSS is severely hindered (Antoni, 2005). A practical solution is to focus on the main vibration source that contributes mostly to the vibration, while it treats all other sources as a combined noise. Then, the objective is reduced to separating the vibration source from noise, which, in this sense, is the cumulative contribution of many different sources. This leads to a blind deconvolution de-noising algorithm (Kundur and Hatzinakos, 1998; Nandi *et al.*, 1997; Peled and Braun, 2005).

Previous research work reported in Patrick (2006) has provided a good understanding of the true vibration signals, originating from the epicyclic gearbox under both healthy and faulty operational conditions. However, little knowledge about the noise profile is available. To remove noise and recover the actual vibration signal, a blind deconvolution algorithm developed for a similarly formulated image-processing problem (Kundur and Hatzinakos, 1998) will be modified and employed. The paper addresses in detail the structure of the overall de-noising scheme, the analysis of vibration mechanisms, the blind deconvolution algorithm, as well as its experimental verification. The results show that the proposed de-noising scheme can substantially improve the signal-to-noise ratio, feature performance and the precision of the failure prognostic algorithm.

2. The de-noising scheme architecture

The proposed overall de-noising scheme is illustrated in Figure 2. An accelerometer mounted on the gearbox frame collects vibration signals and the TSA signal $s(t)$ is calculated. The blind deconvolution de-noising algorithm is carried out in the frequency domain, and hence $s(t)$ is Fourier transformed to arrive at $S(f)$. Then, the de-noising algorithm is applied to $S(f)$, which outputs the de-noised vibration data in the frequency domain $B(f)$. If the time domain signal is required, $B(f)$ can be inverse Fourier transformed to obtain $b(t)$. From $B(f)$ and $b(t)$, features can be extracted and fused to be used subsequently for fault diagnosis and failure prognosis. With the main objective being remaining useful life prediction, the failure prognosis algorithm also provides an estimate of crack length on the planet gear carrier plate as a function of

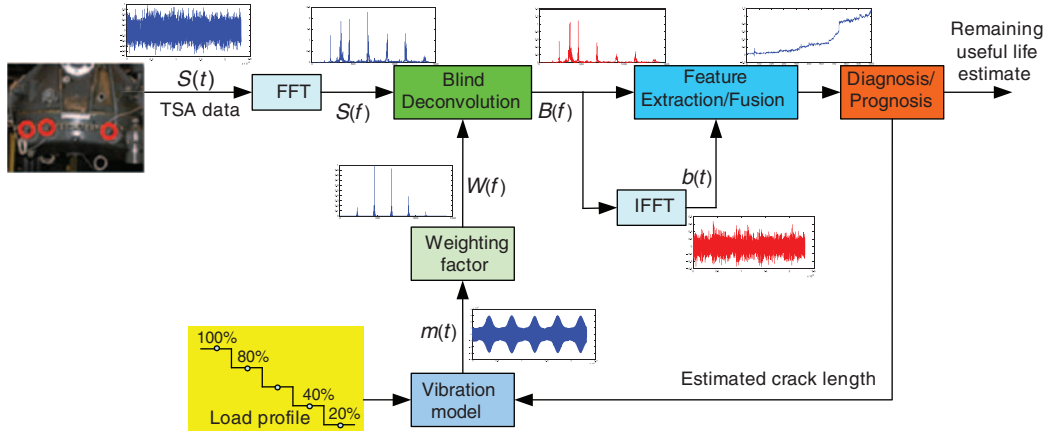


Figure 2 The overall structure of the de-noising scheme

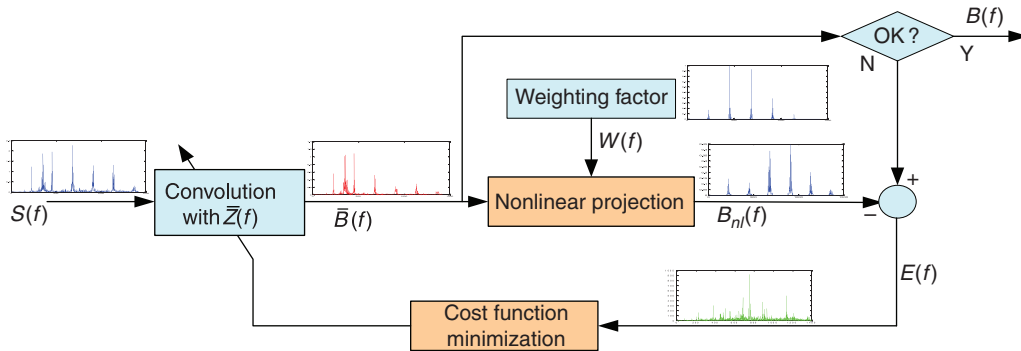


Figure 3 Blind deconvolution de-noising scheme

time (Orchard, 2006). Both the estimated crack length and load profile of the helicopter serve as inputs to the vibration model (Patrick, 2006), which generates the noise-free modelled vibration signal $m(t)$. This modelled vibration signal is Fourier transformed into the frequency domain and its frequency spectra are normalized to obtain the weighting factor vector $W(f)$, which is used in a non-linear projection of the blind deconvolution de-noising algorithm.

The architecture of the proposed de-noising algorithm is decomposed and shown in Figure 3. In this scheme, a non-linear projection, which is based on vibration analysis in the frequency domain, and a cost function minimization are critical components, which are described in the sequel. Initially, an inverse filter $\bar{Z}(f)$ must be defined. This inverse filter is an initial estimate of the modulating signal in the frequency domain, and converges to a filter through an optimization routine that recovers the vibration signal from the noisy measured data $S(f)$. The initial inverse filter $\bar{Z}(f)$ is convoluted

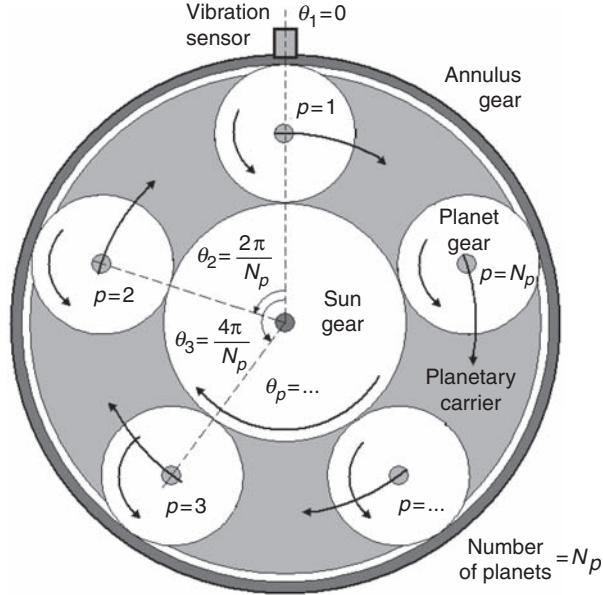


Figure 4 The configuration of an epicyclic gear system

with $S(f)$ to obtain a rough estimate of the noise-free vibration signal $\bar{B}(f)$. The signal $\bar{B}(f)$ passes through the non-linear projection, which maps $\bar{B}(f)$ to a subspace that contains only known characteristics of the vibration signal, to yield $B_{nl}(f)$. The difference between $\bar{B}(f)$ and $B_{nl}(f)$ is denoted as $E(f)$. By adjusting $\bar{Z}(f)$ iteratively to minimize $E(f)$, and when $E(f)$ reaches a minimal value, the signal $\bar{B}(f) \rightarrow B(f)$ can be regarded as the de-noised vibration signal. At the same time, $\bar{Z}(f)$ converges to $Z(f)$. Through an inverse Fourier transform, the de-noised vibration signal in the time domain can be obtained as well.

3. Vibration data analysis

The vibration signals are derived from the main transmission gearbox of Blackhawk and Seahawk Helicopters. The gearbox is an epicyclic gear system with five planet gears, the configuration of which is illustrated in Figure 4. The gearbox is mounted on a test cell, with a seeded crack fault on the planetary gear carrier. The following sections intend to describe the expected vibration data in the healthy and faulty gear carrier plate, respectively.

3.1 Healthy gearbox

Let us assume that the gearbox is an ideal healthy system without cracks. The accelerometer is mounted at a fixed point at position $\theta = 0$. Since the vibration signal is

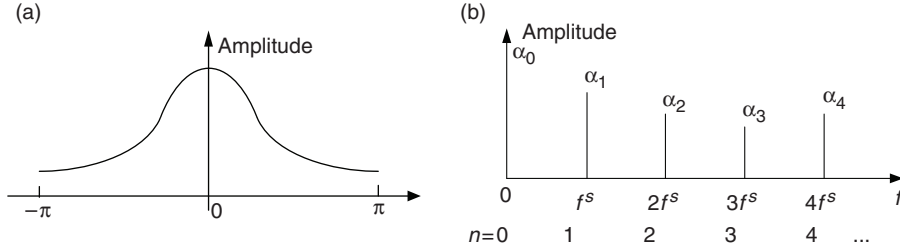


Figure 5 Vibration amplitude modulation signal: (a) time domain modulating signal; (b) frequency domain modulating signal

generated from the meshing of gear teeth and the planetary gears are rotating inside the angular gear, the vibration signal is amplitude-modulated to the static accelerometer. That is, the observed vibration amplitude will be large when the planetary gear is close to the accelerometer and it will be small when the planetary gear is far. Suppose that there is only one planetary gear, then the vibration observed by the transducer should have the largest amplitude when the planetary gear is at $\theta = 0, 2\pi, 4\pi, \dots$. Similarly, the vibration should have the smallest amplitude at $\theta = \pi, 3\pi, 5\pi, \dots$. Suppose that the planetary carrier has a rotation frequency f^s . The vibration amplitude-modulating signal for this single planet gear and its spectra, which show components at harmonics of f^s , are illustrated in Figures 5(a) and (b), respectively. In Figure 5(b), n is the index of harmonics of f^s and α_n is the amplitude of the component of the modulating signal at frequency $n f^s$.

In the ideal case, the $N_p = 5$ planetary gears are evenly spaced. Then, the planetary gear p at time instant t has a phase:

$$\theta_p = 2\pi \left(f^s t + \frac{p-1}{N_p} \right) \quad (1)$$

The amplitude-modulating signal for planetary gear p can be written in the time domain as:

$$a_p(t) = \sum_{n=-N}^N \alpha_n \cos(n\theta_p) \quad (2)$$

where N is the number of sidebands about the harmonics under consideration.

In this case, it is natural to assume that all mesh vibrations generated from different planetary gears are of the same amplitude but of different phase shifts. The annulus gear has $N_t = 228$ teeth. Since the speed at which teeth meshing is proportional to the angular velocity of the planetary carrier, the meshing vibration appears at frequencies $N_t f_s$ (McFadden and Smith, 1985; Patrick, 2006). In addition, supposing that, in the frequency domain, the meshing vibration signal has amplitudes of β_m at its harmonics

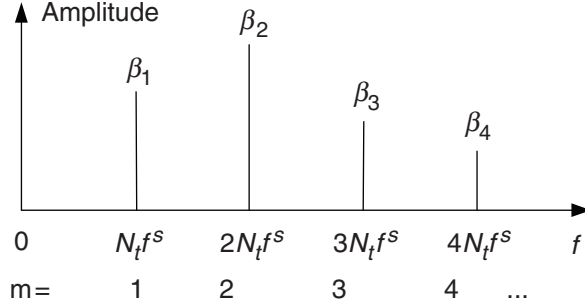


Figure 6 Spectrum of tooth meshing vibration of a single planet gear

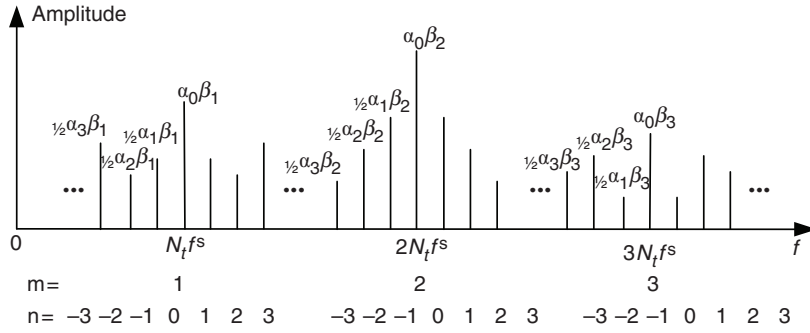


Figure 7 Vibration spectrum of a single planet

$mN_t f_s$, the spectra are illustrated in Figure 6. Then, the vibration signal generated from planet gear p can be written in the form of:

$$b_p(t) = \sum_{m=1}^M \beta_m \sin(mN_t \theta_p) \quad (3)$$

where M is the number of harmonics under consideration.

The observed vibration signal of planetary gear p , with respect to the static accelerometer, is given as the product of the meshing vibration signal and the amplitude-modulating signal. It is denoted as $y_p(t)$, with frequency spectra as shown in Figure 7, and is given by:

$$y_p(t) = a_p(t)b_p(t) = \frac{1}{2} \sum_{m=1}^M \sum_{n=-N}^N \alpha_n \beta_m \sin((mN_t + n)\theta_p) \quad (4)$$

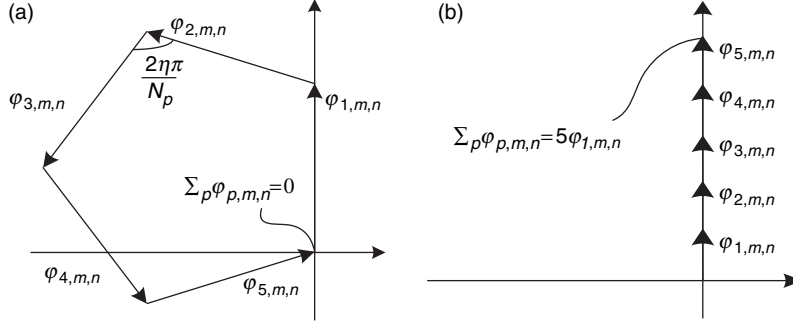


Figure 8 Examples of superposition of vibration signal for a healthy gear plate with $N_p = 5$: (a) $mN_t + n \neq kN_p$ (NonRMC); (b) $mN_t + n = kN_p$ (RMC)

Note the sidebands around the meshing vibration harmonics, compared with Figure 6. The ‘sidebands’ are defined as the frequency components that appear as a harmonically spaced series (McFadden and Smith, 1985; Patrick, 2006). The position of the sidebands can be located by $mN_t + n$ or (m, n) with m being the index of meshing vibration harmonics and n the index of the modulating signal harmonics.

When there are more than one, say N_p , planetary gears, the vibration signal observed by the accelerometer is the superposition of the N_p vibration signals generated from N_p different planetary gears. This superposition vibration signal has the form:

$$\begin{aligned}
 y(t) &= \frac{1}{2} \sum_{p=1}^{N_p} \sum_{m=1}^M \sum_{n=-N}^N \alpha_n \beta_m \sin((mN_t + n)\theta_p) \\
 &= \frac{1}{2} \sum_{p=1}^{N_p} \sum_{m=1}^M \sum_{n=-N}^N \alpha_n \beta_m \sin\left(2\pi(p-1) \frac{mN_t + n}{N_p}\right) \quad (5)
 \end{aligned}$$

where Equation (1) and the fact that $\sin(2k\pi + \theta) = \sin(\theta)$ for any integer k are used.

Since the planetary gears are evenly spaced, the phase angle of the sidebands will be evenly spaced along 2π (McFadden and Smith, 1985). From Equation (5), it is obvious that if sideband $mN_t + n$ is not a multiple of N_p and $(mN_t + n)/N_p$ has a remainder of η , the vibration components from different gears are evenly spaced by an angle $2\eta\pi/N_p$. In this case, when the vibrations generated from different planetary gears are combined, these sidebands add destructively and become zero as illustrated in Figure 8(a), in which $\varphi_{p,m,n}$ with $1 \leq p \leq 5$ indicates the frequency components of gear p . Those frequency components appear at sidebands where $mN_t + n \neq kN_p$ are termed non-regular meshing components (NonRMC).

Conversely, if sideband $mN_t + n$ is a multiple of N_p , the remainder of $(mN_t + n)/N_p$ will be zero. In this case, the vibration components from different gears do not have a

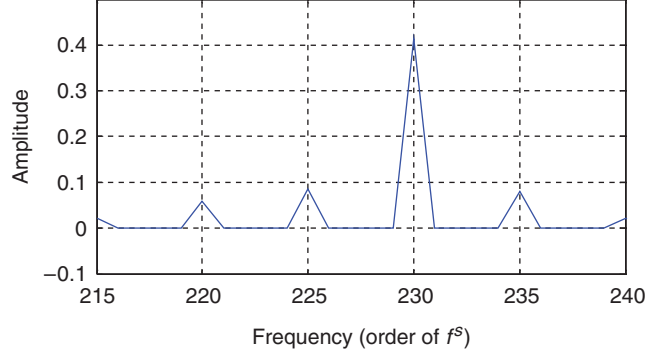


Figure 9 Vibration spectrum of combined signal with $N_t = 228$ and $N_p = 5$

phase difference. When the vibration signals from different planetary gears are combined, these sidebands add constructively and are reinforced as illustrated in Figure 8(b). These frequency components that appear at sidebands where $mN_t + n = kN_p$ are referred to as regular meshing components (RMC) or apparent sidebands.

This process of frequency components adding destructively/constructively finally generates asymmetrical sidebands. Partial frequency spectra of the sidebands around the first-order harmonic that illustrates this asymmetry are shown in Figure 9, where $N_p = 5$ and $N_t = 228$. Note that the peak of the spectrum does not appear at $n = 0$ (order 228) but at $n = -3$ (order 225), $n = 2$ (order 230), etc. The largest spectral amplitude (also known as dominant sideband) appears at the frequency closest to the gear meshing frequency (Keller and Grabill, 2003).

According to the above vibration analysis in the frequency domain and previous research results (Keller and Grabill, 2003; McFadden and Smith, 1985; Patrick, 2006), for an ideal system, only terms at frequencies that are multiples of the number of planetary gears (ie, RMC) survive, whereas the terms at other frequencies (ie, NonRMC) vanish. Then, the Fourier transform of the vibration data can be written as:

$$Y(f) = f_{hea}(\lambda_{m,n}((mN_t + n)f^s)) \quad (6)$$

where $\lambda_{m,n}$ is the magnitude of the spectral amplitude at $(mN_t + n)f^s$ and f_{hea} is the non-linear projection for an ideal healthy gearbox given by:

$$f_{hea} = \begin{cases} 1 & \text{if } mN_t + n \text{ is a multiple of } N_p \\ 0 & \text{otherwise} \end{cases} \quad (7)$$

3.2 Faulty gearbox

When there is a crack on the planetary gear carrier, as in Figure 1, the five gears will not be evenly separated along 2π . Suppose that, at time instant t , one of the five planetary gears has an angle shift δ caused by the crack. Then, this planetary gear has a phase of $\theta_p + \delta$ at time instant t with θ_p being given in Equation (1). For this gear, the modulating signal becomes:

$$a'_p = \sum_{n=-N}^N \alpha_n \cos(n(\theta_p + \delta)) \quad (8)$$

The vibration signal generated from this gear is:

$$b'_p = \sum_{m=1}^M \beta_m \sin(mN_t(\theta_p + \delta)) \quad (9)$$

Accordingly, the modulated vibration signal from this gear is written as:

$$y'_p(t) = a'_p(t)b'_p(t) = \frac{1}{2} \sum_{m=1}^M \sum_{n=-N}^N \alpha_n \beta_m \sin((mN_t + n)(\theta_p + \delta)) \quad (10)$$

If we denote by $\bar{\theta} = 2\pi(p-1)/N_p$, then when the vibration signals from the five planetary gears are superposed (note that the other four gears do not have a phase shift), the observed vibration signal should have the form of (suppose the phase shift happens on the last gear):

$$\begin{aligned} y'(t) &= \frac{1}{2} \sum_{p=1}^{N_p-1} \sum_{m=1}^M \sum_{n=-N}^N \alpha_n \beta_m \sin((mN_t + n)\theta_p) + \frac{1}{2} \sum_{m=1}^M \sum_{n=-N}^N \alpha_n \beta_m \sin((mN_t + n)(\theta_p + \delta)) \\ &= \frac{1}{2} \sum_{m=1}^M \sum_{n=-N}^N \alpha_n \beta_m \left(\sum_{p=1}^{N_p-1} \alpha_n \beta_m \sin((mN_t + n)\bar{\theta}) + \sin((mN_t + n)(\bar{\theta} + \delta)) \right) \end{aligned} \quad (11)$$

Because of this phase shift, when $mN_t + n$ is not a multiple of N_p , the vibration components from different gears are not evenly spaced. This can be illustrated in Figure 10(a). It is obvious that the vibration components are not cancelled in this case. This results in higher NonRMC frequency components. On the other hand, when $mN_t + n$ is a multiple of N_p , the vibration components from different gears are not exactly in phase. The vibration component from the last gear has a phase difference, which results in lower RMC frequency components, as shown in Figure 10(b).

To see this effect in real vibration signals, the frequency spectra around the first harmonic for two different crack sizes at 1.35 inches and 4.4 inches are shown in Figure 11. The components in the circles are the NonRMC. This is consistent with the

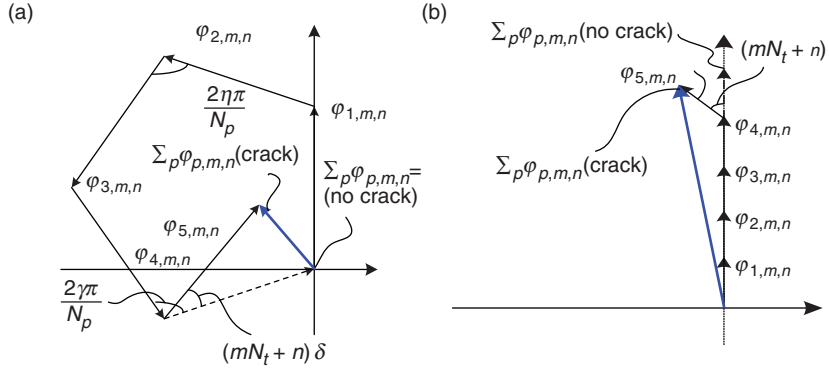


Figure 10 Examples of superposition of vibration signal for a faulty gear plate with $N_p = 5$: (a) $mN_t + n \neq kN_p$ (NonRMC); (b) $mN_t + n = kN_p$ (RMC)

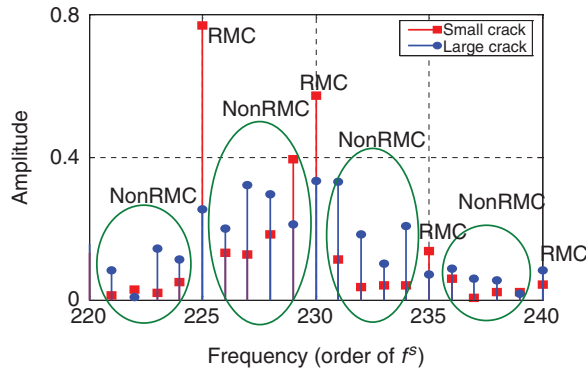


Figure 11 The influence of crack size on frequency spectra

analysis in Figure 10(a). When $(mN_t + n)\delta$ changes from 0 to π , the NonRMC changes from a minimum to a maximum amplitude, whereas the RMC from a maximum to a minimum. On the other hand, when $(mN_t + n)\delta$ changes from π to 2π , the NonRMC becomes from a maximum amplitude to a minimum, whereas the RMC from a minimum to a maximum.

Then, it is clear that the non-linear projection, given in (7), under the assumption of a healthy gearbox, is not suitable for a faulty one. A reasonable modification of the non-linear projection is given as follows. From previous research in Patrick (2006), a vibration model in the frequency domain is established with the load profile and the crack size being two of the inputs. Note that the load profile is known and the crack size can be estimated from the prognostic algorithm (Orchard, 2006). Then, the modelled noise-free vibration signal $m(t)$ generated from the vibration model is

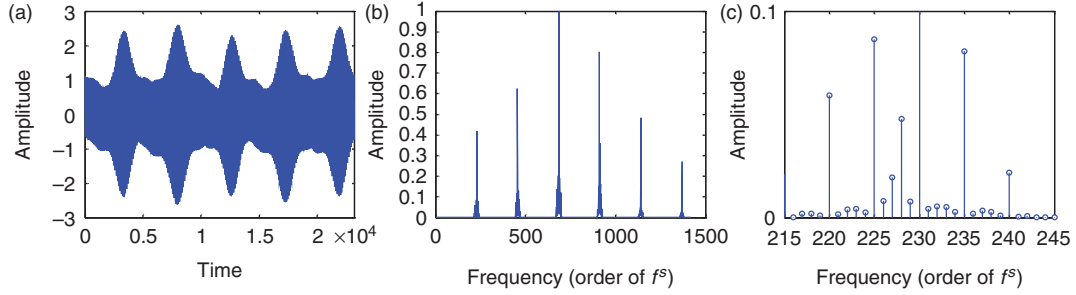


Figure 12 The model vibration signal and weighting factor: (a) the model vibration signal with crack; (b) the weighting factor, normalized model vibration spectra; (c) the weighting factor at the first harmonic

Fourier transformed in the frequency domain to arrive at $M(f)$. The magnitude of $M(f)$ is normalized to obtain weighting factors $W(f)$. For illustration purposes, a model signal $m(t)$ and the weighting factor $W(f)$ derived from its frequency spectra are shown in Figures 12(a) and 12(b). The weighting factors around the first harmonic are zoomed in Figure 12(c).

When a frequency domain signal $\bar{B}(f)$ is fed into the non-linear projection, its frequency components are multiplied by the weighting factor $W(f)$ to arrive at the output of the non-linear projection $B_{nl}(f)$. Suppose that, for a sideband located at $(mN_t + n) f^s$, $\bar{B}(f)$ has a magnitude of $\lambda_{m,n}$, then, after the non-linear projection, the magnitude of $B_{nl}(f)$ at this sideband is given by $W_{m,n}(f)\lambda_{m,n}$, where $W_{m,n}(f)$ is the weighting factor at sideband $mN_t + n$. It is clear that the non-linear projection in this case is:

$$f_{nl} = W_{m,n}(f) \quad \forall (mN_t + n) \in D_{sup} \quad (12)$$

Note that the non-linear projection under the healthy gearbox case in Equation (7) is a special case of (12).

From the above analysis of the system vibration behaviour, the following assumptions are made and used in the blind deconvolution de-noising scheme:

- (1) The majority of vibration information is contained in limited number of sidebands around the harmonics, which form the D_{sup} . Note that the frequency spectra fade quickly on both sides of the harmonics; this assumption is reasonable considering subsequent results.
- (2) The non-linear projection that maps a signal into a subspace contains only known characteristics of the vibration signal is given in (12).
- (3) The amplitude of the modulating signal $a(t)$ decreases monotonically on either side of its maximum value until it reaches the minimum. Note that this assumption is somewhat restrictive.

4. Blind deconvolution de-noising scheme

From the vibration analysis of the gearbox, we know that the vibration signals collected from the transducer are amplitude modulated (McFadden and Smith, 1985; Patrick, 2006). Multiple sources of noise may further corrupt the signal. A simplified model for such a complex signal may be defined as:

$$s(t) = a(t)b(t) + n(t) \quad (13)$$

where $s(t)$ is the noisy vibration signal, $b(t)$ is the noise-free unmodulated vibration signal, $a(t)$ is the modulating signal and $n(t)$ is the cumulative additive noise.

Note that the modulating signal $a(t)$ is itself affected by noise in the system. Let $\hat{a}(t)$ denote the ideal or noise-free modulating signal and $n_a(t)$ the noise introduced in this signal. Consequently, $a(t)$ can be represented as:

$$a(t) = \hat{a}(t) + n_a(t) \quad (14)$$

Thus, Equation (13) can be rewritten as follows:

$$\begin{aligned} s(t) &= (\hat{a}(t) + n_a(t))b(t) + n(t) \\ &= \hat{a}(t)b(t) + \hat{n}(t) \end{aligned} \quad (15)$$

where $\hat{n}(t) = n_a(t)b(t) + n(t)$ contains the total additive noise in the system. On the other hand, the factor $\hat{a}(t)$ describes the multiplicative noise in the system. The goal for a de-noising scheme, such as the one described here, is to recover the unknown vibration signal $b(t)$ from the observed signal $s(t)$, given partial information about the noise sources and characteristics of the vibration signal.

A typical approach would be to find the inverse of $\hat{a}(t)$,

$$\hat{z}(t) = 1/\hat{a}(t) \quad (16)$$

such that

$$\begin{aligned} b(t) &= (s(t) - \hat{n}(t)) \cdot \hat{z}(t) \\ &= s(t)\hat{z}(t) - \hat{n}(t)\hat{z}(t) \end{aligned} \quad (17)$$

Note, however, that little can be assumed about $\hat{n}(t)$ and $\hat{a}(t)$ is not available; $\hat{z}(t)$ is not applicable. To solve this problem, rather than using $\hat{z}(t)$, we propose an iterative de-noising scheme that starts with $\bar{z}(t)$, a very rough initial estimate of the inverse of the modulating signal, which demodulates the observed signal $s(t)$ to give a rough noise-free vibration signal:

$$\bar{b}(t) = s(t) \cdot \bar{z}(t) \quad (18)$$

If partial knowledge about how the plate system is influenced by the modulating signal $\hat{a}(t)$ and a reasonable understanding of the true vibration signal is available, then the ideal characteristics of the vibration signal can be obtained by projecting this

estimated signal $\bar{b}(t)$ into a subspace with only the known ideal characteristics of the vibration signal to yield a refined signal $b_{nl}(t)$. Since this non-linear projection, as the subscript signifies, removes all uncharacteristic components that exist in the rough estimate $\bar{b}(t)$, it is necessary to stress the importance of a good understanding of the underlying process. An iterative scheme then refines these results by minimizing the error between the two signals $\bar{b}(t)$ and $b_{nl}(t)$, ie,

$$\min \|e(t)\| = \min \|\bar{b}(t) - b_{nl}(t)\| \quad (19)$$

Previous research results detail the spectral characteristics of vibration signals for rotating equipment (Keller and Grabill, 2003; McFadden and Smith, 1985; Patrick, 2006). It is appropriate, therefore, to investigate the measured noisy vibration in the frequency domain. The convolution theorem states that the product of two signals in the time domain is equivalent to their convolution in the frequency domain. Thus, model (15) can be written in the frequency domain as:

$$S(f) = \hat{A}(f) * B(f) + \hat{N}(f) \quad (20)$$

with $*$ being the convolution operator and $S(f)$, $\hat{A}(f)$, $B(f)$ and $\hat{N}(f)$ are the Fourier transforms of $s(t)$, $\hat{a}(t)$, $b(t)$ and $\hat{n}(t)$, respectively. Then, the goal in the frequency domain is to recover $B(f)$.

Writing Equation (18) in the frequency domain, we have

$$\bar{B}(f) = S(f) * \bar{Z}(f) \quad (21)$$

with $\bar{B}(f)$ and $\bar{Z}(f)$ being the Fourier transforms of $\bar{b}(t)$ and $\bar{z}(t)$, respectively. Passing $\bar{B}(f)$ through the non-linear projection, it yields $B_{nl}(f)$. Then, in the frequency domain, we will minimize the difference between $B_{nl}(f)$ and $\bar{B}(f)$:

$$\min \|E(f)\| = \min \|\bar{B}(f) - B_{nl}(f)\| \quad (22)$$

The iterative process refines $\bar{Z}(f)$ to minimize Equation (22). When it reaches the minimal value, $\bar{Z}(f)$ converges to $Z(f)$. Then, with this $Z(f)$ replacing $\bar{Z}(f)$ in Equation (21), a good estimate for $B(f)$ is obtained as:

$$B(f) = S(f) * Z(f) \quad (23)$$

Lastly, the estimate is transformed back into the time domain to recover the noise-free vibration signal $b(t)$.

$$b(t) = F^{-1}\{B(f)\} = \int_{-\infty}^{\infty} e^{i2\pi ft} B(f) df \quad (24)$$

To solve this problem, the following additional assumptions are made:

- (1) $Z(f)$ exists and is absolutely summable, ie, $\sum Z(f) < \infty$.
- (2) Since the modulating signal $\hat{a}(t)$ is always positive, its inverse should be positive too.

Hence, the Fourier transform of its inverse $Z(f)$ contains a dc component.

With the above two assumptions being taken into consideration, the cost function is defined as:

$$J = \sum_{f \in D_{sup}} [\bar{B}(f) - B_{nl}(f)]^2 + \left(\sum Z(f) - 1 \right)^2 \quad (25)$$

where D_{sup} is the frequency range that contains the main vibration information. Because of the periodic fade of signal spectra between harmonics, a window centred at harmonic frequencies is used to define critical frequencies. All these windows form the support D_{sup} . In Equation (25), assumptions (4) and (5) are used to arrive at the second term to avoid an all-zero inverse filter $Z(f)$, which leads to the trivial solution for error minimization. Moreover, an iterative optimization routine is required to implement this scheme. The iterative conjugate gradient method is called upon to address the optimization problem. This method has faster convergence rate in general compared with the steepest descent method (Prost and Goutte, 1984).

5. Experimental studies

The initial length of the seeded crack on the carrier is 1.344 inches and it grows with the evolving operation of the gearbox. The gearbox operates over a large number of ground–air–ground (GAG) cycles at different torque levels. This way, vibration data are acquired at different torque levels and different crack lengths.

5.1 Actual crack growth

The ground truth crack length data at discrete GAG cycles are available and tabulated in Table 1. With these data, the crack length for GAG cycles from 1 to 1000 can be obtained via interpolation, which results in the crack length growth curve shown in Figure 13.

5.2 Load profile

In each GAG cycle over the first 320 GAG cycles, the torque increases from 20% to 40%, then to 100%, and finally to 120% and then decreases to 20% for the next cycle. From the

Table 1 The ground truth data of crack length (inches)

GAG	1	36	100	230	400	550	650	714	750	988
Crack	1.34	2.00	2.50	3.02	3.54	4.07	4.52	6.21	6.78	7.63

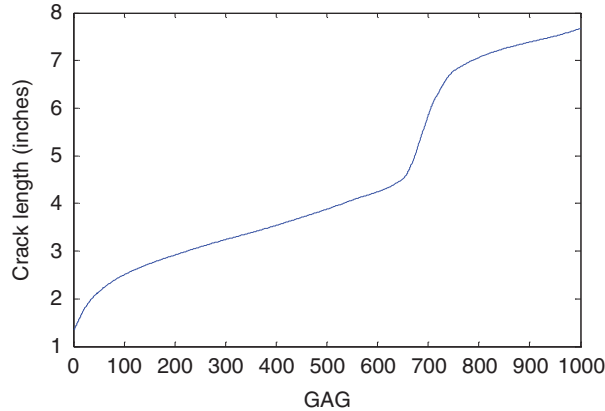


Figure 13 The growth of crack length versus GAG cycles

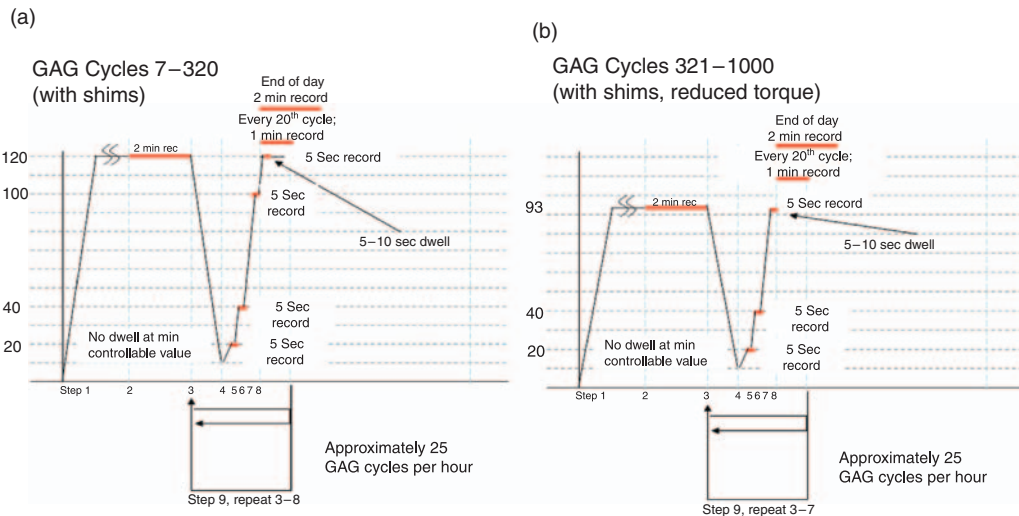


Figure 14 The load profile of the gearbox: (a) GAG cycles 7–320; (b) GAG cycles 321–1000

321st GAG cycle on, the torque in each cycle increases from 20% to 40%, then to 93%, and then decreases to 20% for the next cycle. The torque profiles in these two cases are shown in Figure 14. Because no consistent high torque level data throughout the entire spectrum of GAG cycles is available and there is no substantial difference between the 93% and 100% torque levels, the vibration data at 100% torque in the first 320 GAG cycles and that at 93% torque in the later GAG cycles are considered as consisting one experiment. In this case, torque levels at 20%, 40% and 100% are investigated.

5.3 Online real-time de-noising

It is important to implement the de-noising scheme online. Therefore, the reduction of the computational burden is critical. The real-time implementation of the de-noising scheme involves the structure of the inverse filter $Z(f)$, simplification of the convolution operation, the initial $Z(f)$ and simplification of the optimization routine.

5.3.1 The structure of the inverse filter: For the gearbox with five gears as in Figure 4, the vibration signal observed by the transducer should have its largest amplitude at phase $\theta_i = 0, 2\pi/N_p, 4\pi/N_p, \dots$. The smallest amplitude appears at phase $\theta_i = \pi/N_p, 3\pi/N_p, 5\pi/N_p, \dots$. This indicates that the frequency of the modulating signal $a(t)$ is much lower than that of the vibration signal $b(t)$. The same is true for the inverse of $a(t)$, $1/a(t)$, whose frequency spectra fade quickly at high frequencies. Therefore, at the implementation phase, the inverse filter $\bar{Z}(f)$ can be truncated to a short signal containing only limited coefficients to save computation time and resources. This also helps to improve the efficiency of the algorithm.

5.3.2 Good initial inverse filter: A good initial guess for $\bar{Z}(f)$ will also improve the convergence rate of the blind deconvolution approach. In the process of de-noising, some $Z(f)$ values are collected and saved from previous results. When the system operates under similar operating conditions, the previously saved $Z(f)$ can be retrieved and serves as the initial estimate of $\bar{Z}(f)$ under the current operating condition. It is anticipated that this step will speed up convergence.

5.3.3 Simplification of the optimization routine: Optimization of the de-noising algorithm is a recursive process. The number of iterations is closely related to the required computation time. To reach a minimal value of the cost function, a large number of iterations are needed. However, at the later stages of optimization, the improvement in the cost function value is rather minimal. This suggests that we can terminate the optimization routine before it reaches the minimal value and this will not degrade performance significantly.

For example, the convergence curve of the cost function versus iteration number from a specific example is illustrated in Figure 15. It can be seen that the cost function becomes stable from about the 200th iteration on. Hence, for online applications, the optimization routine can be terminated after a small number of iterations resulting in considerable computational savings.

5.3.4 Simplification of the frequency domain signal convolution: Earlier research results (Patrick, 2006) suggest that the main vibration characteristic signature resides in frequency range below $1500 f^s$ Hz, which covers up to six harmonics. In addition, rapid fade of the signal spectra between the harmonics enable us to define D_{sup} as a series of windows on each side of the harmonics. Therefore, D_{sup} is a collection of six windows

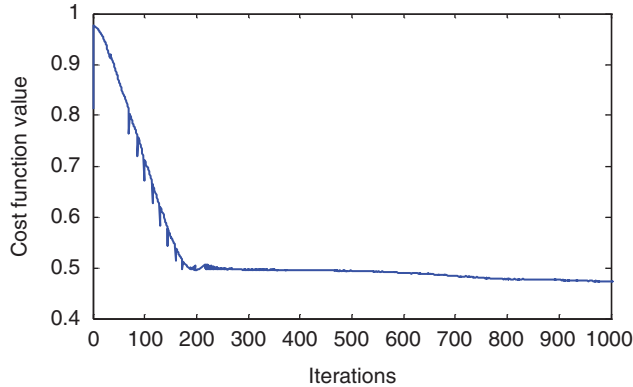


Figure 15 Convergence of cost function along iterations

with each window being centred at the harmonic frequency and having a certain order of sidebands on both sides. Then, the convolution operation only considers frequency spectra on D_{sup} . To achieve this goal, the convolution operation is divided into three steps and this process can reduce the computational burden significantly.

Step 1: Picking up frequency spectra on D_{sup} and separating them into six segments as shown in Figure 16. The original signal spectra are shown in Figure 16(a). The separated spectra at different harmonics are shown in Figures 16(b)–(g).

Step 2: Convoluting each segment with the inverse filter and truncating the convolution results to the length of each segment as illustrated in Figure 17. Figures 17(a) and (b) show the inverse filter and segment of the measured vibration signal (the sidebands at the first harmonic as shown in Figure 16(b), respectively. Figures 17(c) and (d) show the convolution results, before and after the truncation, respectively.

Step 3: Putting the truncated convolution results back to the frequency spectra on D_{sup} to obtain the convolution result.

5.4 Experiments and performance metrics

The signals are normalized and limited within $[-1, 1]$ so that all of them in the proposed scheme can be treated similarly. Since the inverse filter $\bar{Z}(f)$ is a low-frequency signal and we do not assume any prior knowledge, it is truncated to contain only 15 spectral lines and assumed to be a simple discrete impulse located at frequency f^s , as shown in Figure 18(a). The optimal inverse filter $Z(f)$ resulting from the blind deconvolution scheme is shown in Figure 18(b) for comparison purposes. The large frequency components at 5, 10 and 15 are consistent with the modulating signal $a(t)$ for a five-planet-gear plate, whose inverse should show frequency components at 5, 10 and 15, as predicted from the theoretical analysis.

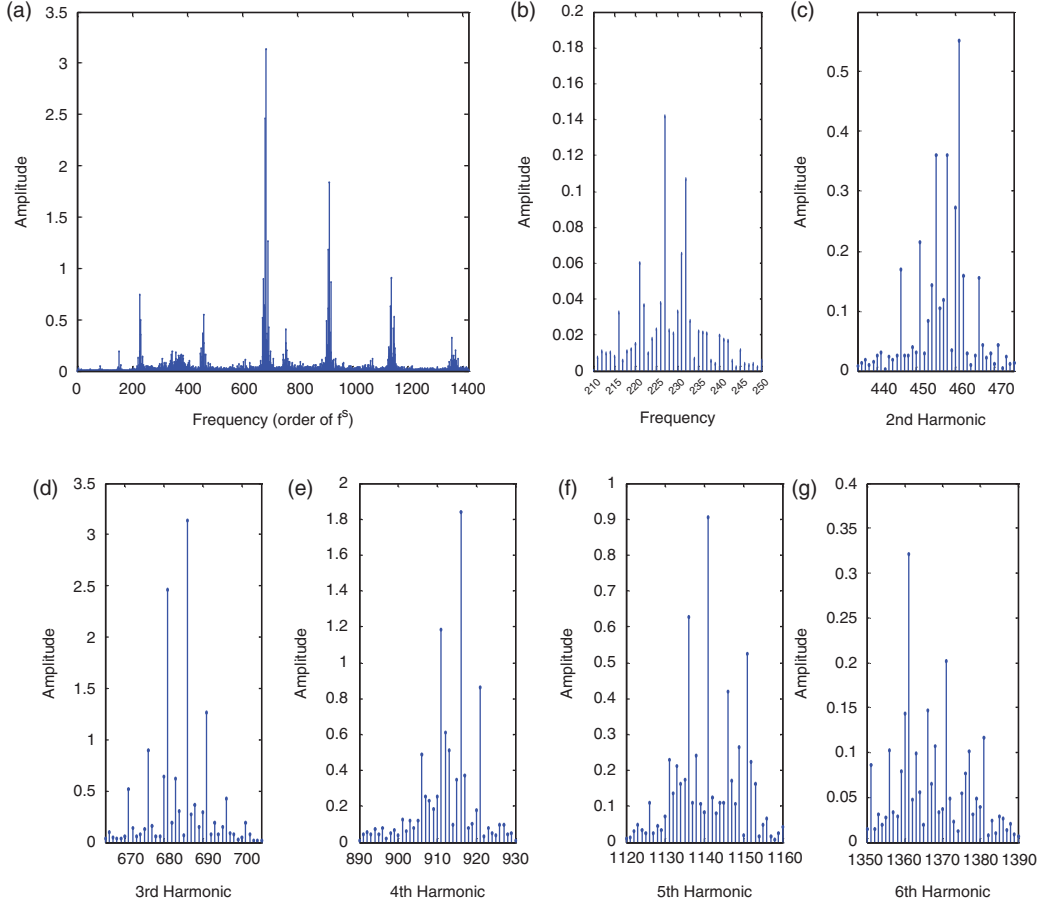


Figure 16 The separation of frequency spectra (with a resolution of f^s): (a) the TSA signal spectra; (b) the first harmonic spectra; (c) the second harmonic spectra; (d) the third harmonic spectra; (e) the fourth harmonic spectra; (f) the fifth harmonic spectra; (g) the sixth harmonic spectra

The non-linear projection is given in Equation (12) and is updated in the closed-loop de-noising scheme, shown in Figure 2, with the varying load profile and crack size. As an example, $\bar{B}(f)$, $B_{nl}(f)$ and their difference $E(f)$ are shown in Figure 19. $E(f)$ is the first term in the cost function (25) that must be minimized through the optimization routine. Finally, in the time domain, the measured noisy vibration signal $s(t)$, the noise-free vibration signal recovered from blind deconvolution $b(t)$ and the noise signal $n(t)$ are shown in Figure 20.

5.4.1 Signal-to-noise ratio: The signal-to-noise ratio (SNR), before and after de-noising, is investigated and the results at 40% and 100% torque levels are

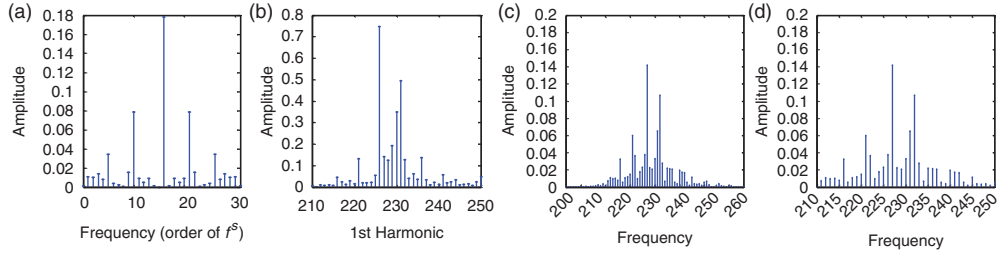


Figure 17 The convolution of the segment of frequency spectra (taking the first harmonic as an example): (a) the inverse filter; (b) the measured vibration signal spectra around the first harmonic; (c) the convolution result; (d) the truncated convolution result

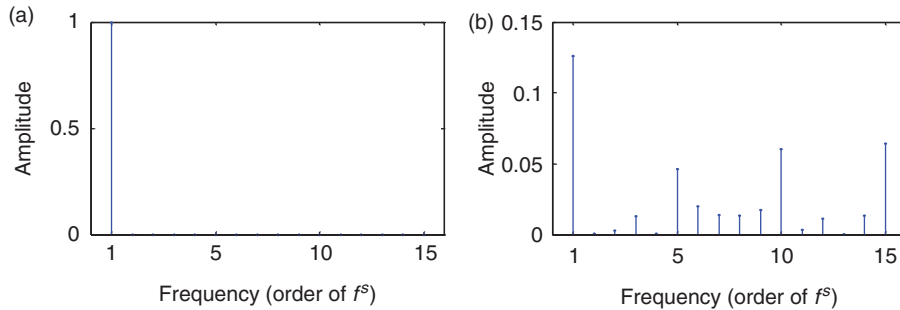


Figure 18 The spectra of the inverse filter: (a) the initial inverse filter; (b) the optimal inverse filter

shown in Figures 21(a) and (b), respectively. The improvement in the SNR value is significant.

5.4.2 Feature performance evaluation: Although the blind deconvolution routine shows a significant improvement in the SNR, it is desirable that it improves also the quality of the features or condition indicators. The accuracy and precision of mappings between the evolution of features and the actual crack growth have an important impact on the performance of diagnostic and prognostic algorithms and the CBM system overall. To evaluate the quality of the features, several performance indexes or metrics are introduced.

The first performance index is an overall accuracy measure defined as the linear correlation coefficient between the raw feature values and the crack length growth along the GAG cycle axis (CCR; Patrick, 2006). Suppose x is the feature vector and

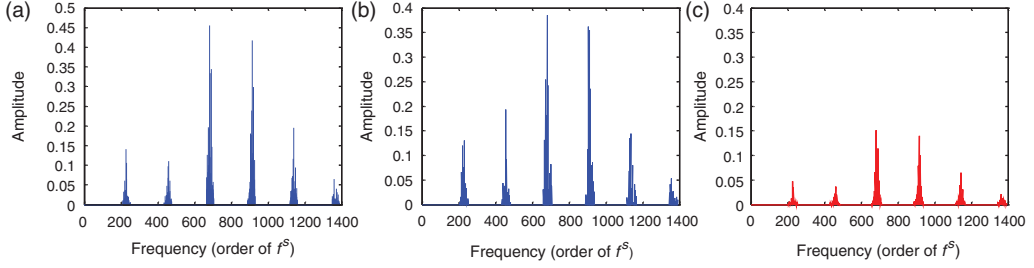


Figure 19 The results of non-linear projection: (a) $\bar{B}(f)$; (b) $B_{nl}(f)$; (c) $E(f)$

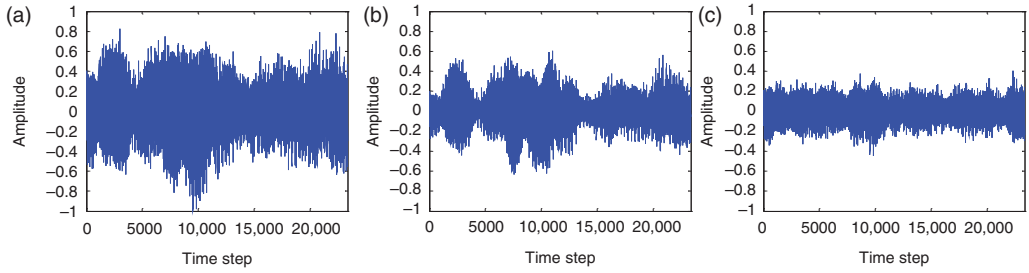


Figure 20 The estimated vibration signal before and after non-linear projection and their difference: (a) the measured vibration signal $s(t)$; (b) the recovered noise-free vibration signal $b(t)$; (c) the noise signal $n(t)$

y the crack growth curve with \bar{x} and \bar{y} their means, respectively. The correlation coefficient between them is:

$$CCR(x, y) = \sqrt{\frac{ss_{xy}^2}{ss_{xx}ss_{yy}}} \quad (26)$$

where $ss_{xy} = \sum (x_i - \bar{x}_i)(y_i - \bar{y}_i)$, $ss_{xx} = \sum (x_i - \bar{x}_i)^2$ and $ss_{yy} = \sum (y_i - \bar{y}_i)^2$, respectively. The extracted feature will be used to map and predict the crack growth. Hence, a high correlation coefficient is expected to generate an accurate estimate of the actual crack length and is preferred. Thus, for a good feature, the value of the correlation coefficient should be near 1.

Because of changes in operating conditions and other disturbances, the feature values along the GAG axis are often very noisy and need to be smoothed through a low-pass filtering operation. In this case, the correlation coefficient is calculated based on the smoothed feature curve \tilde{x} (CCS; Patrick, 2006). The calculation of CCS is the

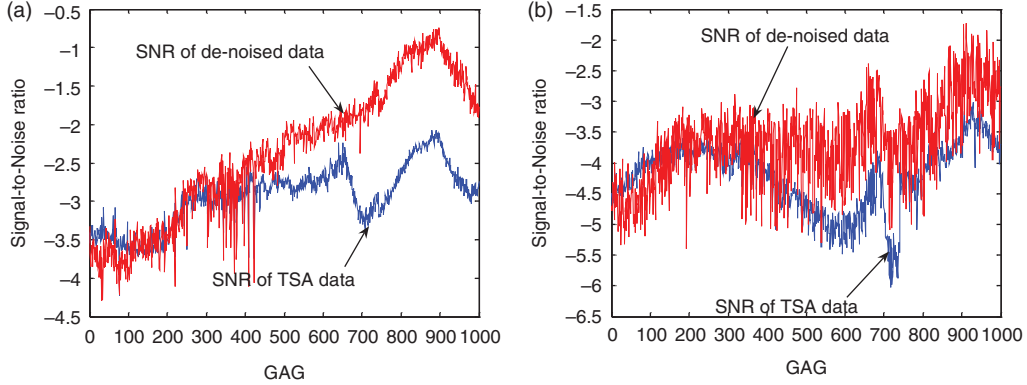


Figure 21 The signal-to-noise ratio: (a) Signal-to-noise ratio at 40% torque; (b) Signal-to-noise ratio at 100% torque

same as (26) with x being replaced by \tilde{x} . In the following experiments, the smooth low-pass filter is a Butterworth filter with cut-off frequency of 0.01 of the sampling frequency.

The third performance index is a precision measure corresponding to a normalized measure of the signal dispersion. It is referred to as percent mean deviation (PMD; Patrick, 2006) and defined by:

$$PMD(x, \tilde{x}) = \frac{\sum_{i=1}^{l_x} \frac{|x_i - \tilde{x}_i|}{x_i}}{l_x} \times 100 \quad (27)$$

where l_x is the number of entities in the feature vector x .

In the fault detection and prognostic algorithms (Orchard, 2006), the extracted feature values are used as a measurement input. Therefore, this performance index is closely related to the detection threshold and precision of the prognosis results (remaining useful life). From a precise feature, the fault detection and prognostic algorithms can detect the incipient failure and/or predict the fault growth with a high confidence. PMD for a precise feature should have a very small value close to 0.

The previous indexes evaluate the performance on the entire failure progression process. It is also important to evaluate how the failure progresses in a small period. To achieve this goal, a moving window along the time axis is applied to the feature vector so that the correlation coefficient and PMD in the moving windows can be evaluated to provide a 'local' performance assessment. The two adjacent windows are overlapped so that the performance indexes in this case are curves along the time axis.

The relative size of the NonRMC sidebands to the RMC sidebands in D_{sup} or part of D_{sup} may indicate the presence of a fault on the planetary carrier. As the crack grows, the operating conditions deviates from the ideal. In this case, the constructive superposition of vibration signals from different planetary gears is attenuated while

the destructive superposition is reinforced. This phenomenon results in smaller RMC and larger NonRMC sidebands. This indicates that the ratio between RMC and NonRMC sidebands can be used as a characteristic feature. Based on this notion, features are successfully extracted in the frequency domain. One of these features, the sideband ratio (SBR; Wu *et al.*, 2004), will be used to demonstrate the effectiveness of the de-noising routine.

Let X denote the number of the sidebands in consideration on both sides of the dominant components of the harmonics, the sideband ratio is then defined as the ratio between the energy of the NonRMC and all sidebands:

$$SBR(X) = \frac{\sum_{h=1}^m \sum_{g=-X}^X NonRMC}{\sum_{h=1}^m \sum_{g=-X}^X (NonRMC + RMC)} \quad (28)$$

The results of SBR(12) at 40% torque level are shown in Figure 22(a). The running version of the performance indexes is shown in Figure 22(b). The results at 100% torque are shown in Figures 22(c) and 22(d), respectively.

The correlation coefficient and PMD for this feature at different torque levels are summarized in Table 2. Substantial feature improvements are achieved via the application of the de-noising routine. In the tables, D-N stands for de-noised.

5.4.3 Failure prognosis: A fault detection/failure prognosis framework based on particle filtering algorithms has been successfully developed, and applied to the prediction of the remaining useful life (RUL) of the critical components (Orchard, 2006). The approach provides with a particle-filter-based estimate of the state probability density function (pdf), generates p -step ahead long-term predictions and uses available empirical information about hazard thresholds to estimate the RUL pdf. The implementation of this algorithm requires a failure progression model, feature measurements to reveal the failure progression, a non-linear mapping between failure severity and feature value, and external inputs such as the operational load profile to the system. More details about this prognosis framework can be found in Orchard (2006). In this section, results are shown to compare the algorithm performance when using the features derived in the previous section, before and after de-noising. This will illustrate the efficiency of the proposed de-noising routine, on the prediction of the planetary carrier RUL in the helicopter testbed.

Once the RUL pdf is calculated, the performance of failure prognostic algorithm can be evaluated. For this purpose, statistics such as 95% confidence intervals (CI) and RUL expectations may be used. In our experiment with a seeded crack on the planetary carrier, failure is defined when the crack reaches 6.21 inches in length, ie, the crack reaches the edge of the carrier plate. The ground truth data in Table 1 show that the crack size reaches this value at the 714th GAG cycle.

Since the gearbox operates on the basis of GAG cycles, the RUL expectations and 95% CI are also given with the unit of 'GAG cycle'. Long-term predictions are

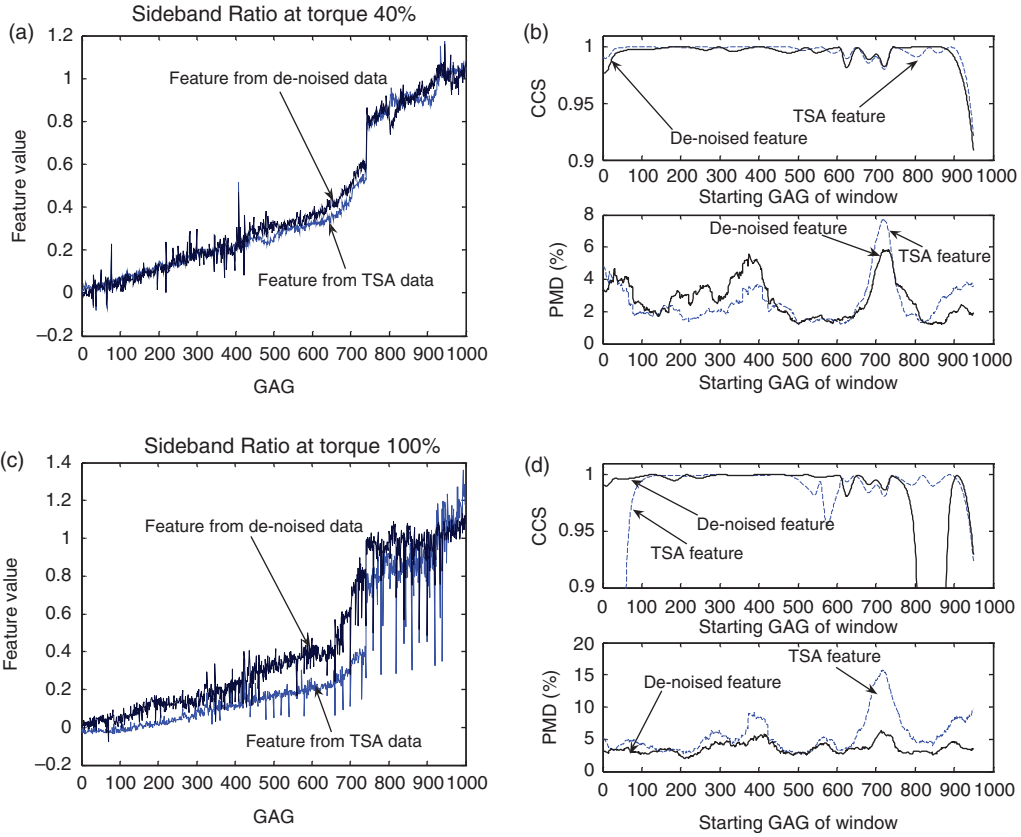


Figure 22 Feature SBR(12) before and after de-noising: (a) SBR(12) at 40% torque; (b) running CCS and PMD; (c) SBR(12) at 100% torque; (d) running CCS and PMD

Table 2 The performance indexes of feature Sideband Ratio

Torque	20%		40%		100%	
	TSA	D-N	TSA	D-N	TSA	D-N
CCR	0.943	0.975	0.979	0.985	0.953	0.983
CCS	0.950	0.982	0.986	0.992	0.971	0.991
PMD	2.06%	2.01%	2.57%	2.73%	5.57%	3.57%

generated at the end of the 365th GAG cycle, using the current estimate for the state pdf as initial condition. The state pdf estimate, in turn, is based on feature measurements considering two cases: before and after the de-noising routine. Results for each case are depicted in Figures 23(a) and (b), respectively. It must be

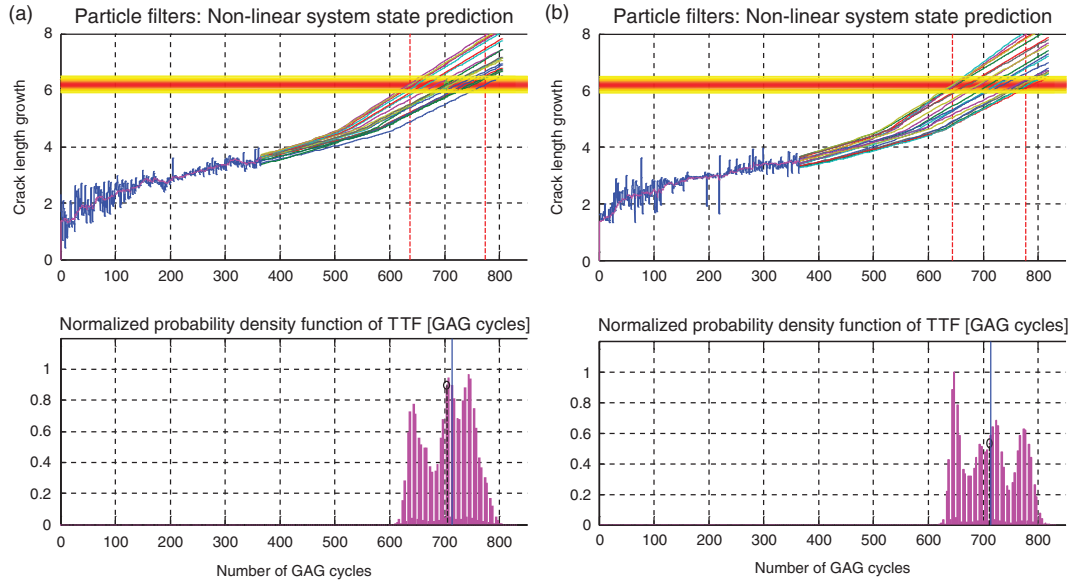


Figure 23 Prognosis results started from the 365th GAG cycle:
 (a) prognosis based on TSA feature; (b) prognosis based on de-noised feature

Table 3 The performance indexes of failure prognosis

Feature	Performance	Initial GAG cycle for long-term prediction			
		365	400	450	500
TSA	95% CI	[637–773]	[663–832]	[680–828]	[682–812]
	Length of CI	136	169	148	130
	Expected value	705	747	754	747
De-noised	95% CI	[638–777]	[647–775]	[618–720]	[695–784]
	Length of CI	139	128	102	89
	Expected value	710	711	670	746

noted that the 95% CI in both scenarios are quite similar precision-wise. However, the RUL expectation is closer to the ground truth value when a de-noised feature is used, showing that the de-noise routine improves the accuracy of the algorithm.

As time goes on, differences between the two cases become evident. Table 3 summarizes the results obtained when performing the prognostic algorithm at the 400th, 450th and 500th GAG cycles, respectively. In terms of precision of the prediction, it is clear that prognosis results with the de-noised feature offer a considerable reduction in the length of the 95% CI. For instance, when the long-term prediction is

performed at the 450th GAG cycle, this reduction is in the order of about 140 min (46 GAG cycles). At the same time, the expected values for the RUL obtained from the de-noised feature are also more accurate than those from the TSA feature. It is important to note that, in real applications, a predicted failure time lower than the actual one is preferred since it does not involve the risk of continuing the operation beyond safety. A lower failure time prediction only makes a conservative decision to schedule maintenance earlier, but a higher value of the failure time in the prediction might postpone the timely maintenance, resulting in damage or loss of vehicle.

6. Conclusions

The successful implementation of CBM technologies is achieved through the application of a failure prognostic algorithm, which in turn requires a high-quality feature to propagate the failure in time with respect to the operating conditions of the system. Good features are often extracted from vibration signals collected from a noisy environment and noise might mask the signatures of the faults/failures. Therefore, signal de-noising and preprocessing is important in the implementation of CBM. This paper introduces the development of a new vibration signal blind deconvolution de-noising scheme in synergy with feature extraction, failure prognosis and vibration modelling to improve the signal-to-noise ratio, the quality of features, as well as the accuracy and precision of failure prognostic algorithms. The proposed scheme is applied to the failure prognosis of a critical component of a helicopter testbed and the results demonstrate the efficiency of the proposed scheme.

Acknowledgements

The research reported in this paper was partially supported by DARPA and Northrop Grumman under the DARPA Prognosis program Contract No. HR0011-04-C-003. We gratefully acknowledge the support and assistance received from our sponsors.

This paper should have been included in the themed issue on diagnostics and prognostics that was published in the June–August double issue 2009, volume 31 issue 3–4.

References

- Antoni, J.** 2005: Blind separation of vibration components: principles and demonstrations. *Mechanical Systems and Signal Processing* 19, 1166–80.
- Antoni, J.** and **Randall, R.** 2004: Unsupervised noise cancellation for vibration signals: part I – evaluation of adaptive algorithms. *Mechanical Systems and Signal Processing* 18, 89–101.
- Ayers, G.R.** and **Dainty, J.C.** 1988: Iterative blind deconvolution method and its applications. *Optics Letters* 13, 547–49.
- Gelle, G., Colas, M.** and **Delaunay, G.** 2000: Blind sources separation applied to rotating machines monitoring by acoustical and vibrations analysis. *Mechanical Systems and Signal Processing* 14, 427–42.
- Hillerstrom, G.** 1996: Adaptive suppression of vibrations – a repetitive control approach, *IEEE Trans. Control Systems Technology* 4(1): 72–78.
- Keller, J.** and **Grabill, P.** 2003: Vibration monitoring of a UH-60A main transmission planetary carrier fault. *The American Helicopter*

- Society 59th Annual Forum*, Phoenix, AZ, May, 1–11.
- Klamecki, B.** 2005: Use of stochastic resonance for enhancement of low-level vibration signal components. *Mechanical Systems and Signal Processing* 19, 223–37.
- Kundur, D. and Hatzinakos, D.** 1998: A novel blind deconvolution scheme for image restoration using recursive filtering. *IEEE Transactions on Signal Processing* 26, 375–90.
- Lebold, M., McClintic, K., Campbell, R., Byington, C. and Maynard, K.** 2000: Review of vibration analysis methods for gearbox diagnostics and prognostics. *Proceedings of the 54th Meeting of the Society for Machinery Failure Prevention Technology*, Virginia Beach, VA, May, 623–34.
- McFadden, P. and Smith, J.** 1985: An explanation for the asymmetry of the modulation sidebands about the tooth meshing frequency in epicyclic gear vibration. *Proceedings of the Institution of Mechanical Engineers, Part C: Mechanical Engineering Science* 199, 65–70.
- Nandi, A.K., Mampel, D. and Roscher, B.** 1997: Blind deconvolution of ultrasonic signals in nondestructive testing applications. *IEEE Transactions on Signal Processing* 45, 1382–90.
- Orchard, M.** 2006: A particle filtering-based framework for online fault diagnosis and failure prognosis. PhD proposal, School of Electrical and Computer Engineering, Georgia Institute of Technology, Atlanta, GA.
- Patrick, R.** 2006: A model-based framework for fault diagnosis and prognosis of dynamical system with an application to helicopter transmissions. PhD proposal, School of Electrical and Computer Engineering, Georgia Institute of Technology, Atlanta, GA, September.
- Peled, M.Z.R. and Braun, S.** 2005: A blind deconvolution separation of multiple sources, with application to bearing diagnostics. *Mechanical Systems and Signal Processing* 19, 1181–95.
- Prost, R. and Goutte, R.** 1984: Discrete constrained iterative deconvolution with optimized rate of convergence. *Signal Processing* 7, 209–30.
- Saxena, A., Wu, B. and Vachtsevanos, G.** 2005: A methodology for analyzing vibration data from planetary gear system using complex Morelet wavelets. *Proceedings of the American Control Conference*, vol. 7, Portland, OR, June, 4730–35.
- Szczepanik, A.** 1989: Time synchronous averaging of ball mill vibrations. *Mechanical Systems and Signal Processing* 3, 99–107.
- Vachtsevanos, G., Lewis, F., Roemer, M., Hess, A. and Wu, B.** 2006: *Intelligent fault diagnosis and prognosis for engineering systems*. Wiley.
- Wu, B., Saxena, A., Khawaja, T., Patrick, R., Vachtsevanos, G. and Sparis, R.** 2004: An approach to fault diagnosis of helicopter planetary gears. *IEEE AUTOTESTCON*, San Antonio, TX, September, 475–81.
- Wu, B., Saxena, R.P.A. and Vachtsevanos, G.** 2005: Vibration monitoring for fault diagnosis of helicopter planetary gears. *IFAC World Congress*, Prague, July.